

SPECIAL ISSUE ARTICLE OPEN ACCESS

Physics-Based Machine Learning Electroluminescence Models for Fast yet Accurate Solar Cell Characterization

Erell Laot^{1,2,3}  | Jean-Baptiste Puel^{1,2} | Jean-François Guillemoles^{3,4}  | Daniel Ory^{1,2} 

¹EDF R&D, Palaiseau, France | ²Institut Photovoltaïque d'Ile-de-France (IPVF), Palaiseau, France | ³Institut Photovoltaïque d'Ile-de-France (IPVF), UMR 9006, CNRS, Ecole Polytechnique—IP Paris, Chimie Paristech—PSL, Palaiseau, France | ⁴Chimie Paristech - PSL, Ecole nationale supérieure de chimie de Paris, Paris, Île-de-France, France

Correspondence: Erell Laot (erell.laot@edf.fr)

Received: 29 June 2024 | **Revised:** 28 October 2024 | **Accepted:** 6 February 2025

Funding: This work was supported by the French National Research Agency (ANR) (ANR IEEED-002-01) and by the Association Nationale de la Recherche et de la Technologie (ANRT) (Convention CIFRE ANRT-EDF 2023/1124).

Keywords: electroluminescence | imaging | machine learning | neural network | photovoltaic | regression | U-NET

ABSTRACT

Electroluminescence analyses of solar cells and modules allow for fast, cost-effective, and nondestructive spatial characterization of devices at different stages of their development and use. Voltage-dependent electroluminescence (ELV) measurements have been shown to mimic diode voltage–current characteristics. A derived physical model enables the determination of two local pseudoparameters from ELV data measured on silicon solar cells: a pseudorecombination current J_0^* and a pseudoseries resistance R_s^* . Local characteristics of the solar cells, such as the series resistance R_s or the dark saturation current J_0 , can be deduced from these pseudoparameters. ELV measurements are stored in large data cubes, typically containing a few hundred thousand pixels. Pixel-wise regression is commonly achieved through nonlinear least squares (NLLS) minimization; knowing that a luminescence image of a 6" silicon solar cell contains about 1 Mpix, this method is time-consuming, necessitating a trade-off between sample size, spatial resolution, fitting accuracy, and computation duration. We hence propose to replace NLLS fitting with machine learning (ML) techniques, known for their efficiency in rapidly processing large datasets. We compare the regression performances of a multilayer perceptron (MLP) with the ones of a convolutional neural network (CNN) called modified U-NET (mU-NET). The first ML model conducts a pixel-wise analysis of the data cube and the second processes the entire data cube in a single step. We present a comprehensive characterization of prediction accuracy, objectively assessing the advantages and limitations of the proposed techniques. Our first step is to ensure that the prediction precision is sufficient for a valid comparison of the analysis duration. The deviation of accuracy of these models compared to NLLS is almost negligible for MLP and of 3.1% when employing mU-NET, demonstrating their relevancy for operational application. Both ML models are fast and efficient: the time required for regression decreases by a factor of 240 with the MLP and by a factor of 1200 with the mU-NET, compared to the NLLS method.

1 | Introduction

Reducing carbon dioxide emissions is necessary to fight against climate change and global warming. That is the reason why photovoltaic (PV) energy systems, that are low

carbon energy supply technologies, have an increasing weight in the electricity generation mix worldwide. Improving PV device power conversion efficiency (PCE), lifetime, reducing their cost and energy payback time are key to increase PV production and installation. The characterization of solar cells

This is an open access article under the terms of the [Creative Commons Attribution License](#), which permits use, distribution and reproduction in any medium, provided the original work is properly cited.

© 2025 The Author(s). Progress in Photovoltaics: Research and Applications published by John Wiley & Sons Ltd.

and modules optoelectronic properties is then fundamental to understand and find solutions against losses and degradation mechanisms.

The physical characterization of solar cells can be performed at various levels and across various dimensions. Current–voltage (IV) characteristics constitute the predominant 1D characterization method for solar cells, enabling the assessment of cells' health by measuring parameters such as short-circuit current, open-circuit voltage, and maximum power point. This approach further plays a crucial role in fault diagnosis [1–5] and enables the derivation of key parameters reflecting cell defects and losses [6–8], including series resistance R_s , shunt resistance R_{sh} , and saturation current J_0 . Other techniques, such as the analysis of the average photoluminescence (PL) spectra emitted by solar cells or temperature- and injection-dependent lifetime spectroscopy (TIDLS) are, respectively, useful in characterizing parameters like quasi-Fermi level splitting (QFLS) and bandgap [9] or for the identification of defect features [10]. We listed several 1D characterization techniques that are powerful tools for defect and performance characterization but do not allow for the detection of specific defective region.

Spatially resolved characterization techniques are a solution to overcome this limit. They enable a thorough examination of the factors impacting solar cell efficiency and facilitate the study of inhomogeneity effects. These techniques utilize both 2D and 3D measurements. Notably, nondestructive luminescence techniques are extensively utilized. PL measurements can be conducted at any stage of fabrication, whereas electroluminescence (EL) measurements are only feasible after contacting the solar cell. Single EL images are utilized for defect detection [11] and classification [12]. Additionally, they have been employed for predicting the maximal power point of solar cells [13] and for local estimation of parameters such as the parallel conductance [14]. Pairs of PL [15] or EL images [14, 16] have been utilized for estimating local parameters such as the saturation current $J_0(r)$ and the series resistance $R_s(r)$. Advanced characterization techniques, including 3D measurements or combinations of methods, as those described in [17, 18] using PL, EL, and IV measurements to predict local saturation current and resistance, are employed for comprehensive analysis of solar cells. Hyperspectral PL measurements are utilized to estimate local bandgaps [19] and QFLS [20] and hyperspectral EL for diffusion length [21], while voltage-dependent EL (ELV) technique is used for absolute determination of the local values of $R_s(r)$ and $J_0(r)$ [22].

We focus on two groups of techniques used to extract parameters from experimental measurements, as those previously presented, using physical models. The first group includes fitting techniques that optimize parameter values by minimizing (or maximizing) an objective function, such as the mean squared error (MSE) or the mean absolute error (MAE), comparing the experimental data with the modeled data which is a function of these parameters. This group, that notably includes nonlinear least squares (NLLS) fitting, is an important and dynamic area of investigation [23]. The second group involves deriving a function that inverts the physical model, enabling direct prediction of parameter values from experimental measurements. This group encompasses machine learning (ML) techniques

that learn the relationship between measurements (inputs) and parameters of interest (outputs).

ML techniques can be used to process 1D data, both for classification and regression purposes. Based on a feature vector extracted from light intensity-dependent IV characteristics, the dominant recombination process in perovskite solar cells is identified using a random forest model trained on synthetic data generated through drift-diffusion simulations in [24]. The ability of different ML models to extract defect parameters (energy level, capture cross-section ratio) in silicon wafers from TIDLS were compared in [10]. In [25], an artificial neural network (ANN) is combined with a numerical current predictor (NCP) to predict several parameters of the single-diode model from IV measurements.

ML is equally well suited for handling larger dimensional data: It has been widely used in the recent years for a large range of imaging applications such as pixel-wise data classification (segmentation) for medical [26, 27], land analysis [28–30], and applications or phase classification in battery [31], for instance. It has also been adopted by the PV community for processing both 2D and 3D data types. In [32], a convolutional neural network (CNN) called U-NET is coupled with physical constraints to predict J_0 maps and the open-circuit voltage V_{OC} from PL images. In [33], an ensemble of CNNs is used to estimate various parameters along with their uncertainty from EL images. In [34], U-NET is used for segmentation of EL images; two types of defects (J_0 and R_s defects) are locally identified.

The performance of NLLS fitting methods, such as the trust reflective region (TRR) algorithm, has been compared with ML approaches in several publications. [35, 36] compared the TRR with regression neural networks (NNs) and obtained better results with the NNs for some parameters estimation. Indeed, the use of a multilayer perceptron (MLP) resulted in a smaller agreement interval on the estimated parameter of interest in [36], additionally several error estimators were improved using a CNN to compute spatially resolved features from data cubes in [35].

In this study, we will focus on the estimation of the local series resistance $R_s(r)$ and the local dark saturation current $J_0(r)$ of silicon solar cells using the ELV imaging method already mentioned [22]. ELV measurements present a similarity with IV characteristics, and it is possible to extract locally two pseudoparameters, a pseudoseries resistance R_s^* , and a pseudosaturation current J_0^* from ELV data cubes. Those parameters are related to the local R_s and J_0 . The standard approach to derive the pseudoparameters from ELV data cubes is NLLS minimization, which is generally reliable but presents several limitations: First, optimization must be performed individually for each ELV curve corresponding to a spatial pixel, resulting in significant time consumption when dealing with a large number of pixels. Second, the accuracy of the results is highly dependent on the initialization of parameters, which can affect the algorithm's performance. To overcome these limits, we propose to use ML-based regression techniques. We will compare the performances of MLPs, performing a pixel-wise analysis of the data similarly to NLLS, and of CNNs, more precisely modified U-NET (mU-NET) architectures, that process the whole data cube at once. These three regression methods (NLLS, MLP, and mU-NET) were selected for their high generalizability and their ability

to operate without imposing constraints on the physical model. To quantify the advantages of using ML compared to NLLS, several performance indicators are studied, namely, the regression precision and the prediction time. We will firstly show that the ML prediction results are close to the ones obtained utilizing NLLS fitting and secondly establish that the different regression methods allow to precisely fit the data, the MLP being almost as accurate as NLLS fitting. We will then demonstrate how the use of ML reduces the analysis duration, showing that significantly faster regression is achievable while maintaining high precision. Subsequently, we will discuss the extent to which the models should be optimized, given the presence of noise in the studied data. Ultimately, we will consider the effect of the thermal voltage in the ELV model and emphasize that a low fitting error does not sufficiently guarantee the physical significance of the results.

2 | Results and Discussion

In this section, we will describe the physical model at stake and then go into details of the performance of the ML models we selected. This performance will be evaluated at different stages. First, we will assess the prediction ability on synthetic data. Then, the intermediate parameters obtained by applying our ML models on experimental data will be compared to the ones already calculated using NLLS. Third, the quality of reconstruction of the experimental ELV curves acquired will be evaluated. Finally, the physically relevant characteristics expected from the physical model will also be compared, assessing the interest and quality of ML versus NLLS.

2.1 | ELV Model and Sample

ELV measurements have been shown to mimic local diode IV characteristics [22]. Figure 1a compares the IV characteristic to the average ELV measured on a silicon solar cell and emphasizes the resemblance between the two phenomena. A corresponding physical model (Equation 1) enables the derivation of three local parameters from ELV data measured on silicon solar cells: a pseudorecombination current J_0^* , a pseudoseries resistance R_s^* ,

and a pseudothermal voltage v_{th}^* . The parameter R_s^* is a lumped pseudoresistance connecting the local points (pixels) to the terminal contacts.

$$EL(V_T) = J_0^* \times \exp\left[\frac{V_T - R_s^* \times EL}{v_{th}^*}\right]. \quad (1)$$

V_T is the terminal voltage in volts, that is, the bias applied to the cell. v_{th}^* is the pseudothermal voltage:

$$v_{th}^* = n_{id}^* \times v_{th}, \quad (2)$$

with $v_{th} = \frac{k_B T}{q}$ the thermal voltage where q is the elementary charge, k_B is the Boltzmann constant, and T is the temperature in Kelvin. n_{id}^* is the pseudoideality factor of the cell, assumed to be 1, as in [22]. The cells' temperature is regulated at 295 K during ELV measurements.

R_s^* and J_0^* are in arbitrary unit. The calibration matrix of the measurement setup (that depends on the optical path, the camera conversion factor, the pixel surface, and the acquisition time) and the quantum efficiency of the camera allows to compute the absolute EL intensity (in photon counts) emitted by the sample and to link the pseudoparameters with values in the international system of units. Indeed, various local characteristics of the solar cells, such as the series resistance R_s and the dark saturation current J_0 , can be deduced from the pseudoparameters R_s^* and J_0^* , provided that some of the cell's parameters, such as the doping or the diffusion coefficient, are known. The method to determine R_s and J_0 from R_s^* and J_0^* has been thoroughly described in [22] and is summarized in Section 5.1. We emphasize that R_s^* and R_s , as well as J_0^* and J_0 , are distinct and should not be confused. Remarkably, the relationship between J_0 and J_0^* is nonlinear, with J_0 increasing inversely with J_0^* .

The EL intensity map measured under a 690-mV voltage bias on an aluminum back surface field (Al-BSF) silicon solar cell with a high dislocation concentration is shown in Figure 1b. The area delimited by the red rectangle in this figure will serve as

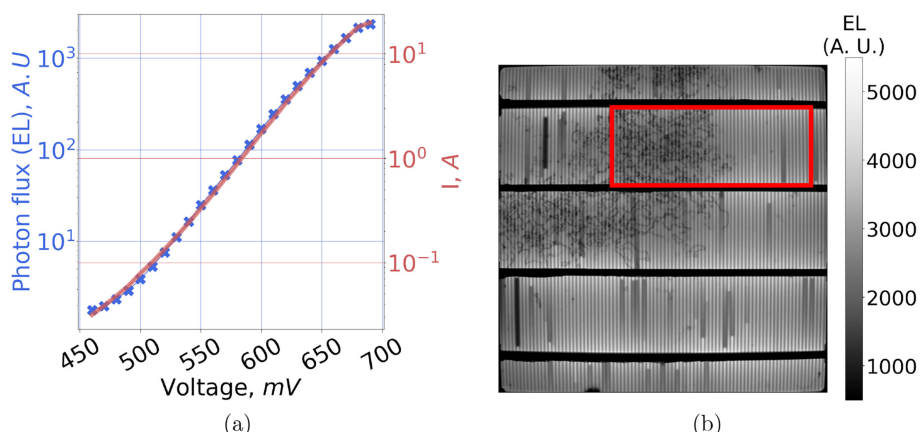


FIGURE 1 | (a) Average electroluminescence (EL) signal measured on an Al-BSF silicon solar cell under increasing voltage bias (blue crosses) and current-voltage characteristic of the same cell (red line). (b) EL intensity map measured at a 690-mV bias, the resolution is of $306 \times 306 \mu\text{m}^2$ per pixel. The red rectangle delimits a region of interest that will be studied in this paper. [Color figure can be viewed at wileyonlinelibrary.com]

a reference in the following sections, and some results will be presented for this region only. The R_s^* and J_0^* ML-predicted maps corresponding to this region are presented in Figure 2.

EL intensity maps, such as the one in Figure 1b, show the presence of metallic contacts and defects. Two types of metallic contacts are distinguishable: The busbars, appearing as large dark horizontal bands, conduct the current from the fingers to the external circuits, while the thinner, perpendicular fingers collect the current from the cell surface.

On EL maps, dislocations appear as very thin dark filaments on a brighter background, where R_s^* is higher and J_0^* lower than rest of the cell; see Region 1 in Figure 2a,b. Damaged fingers are also identifiable on EL intensity maps by thin dark rectangle areas perpendicular to the busbars. They are characterized by

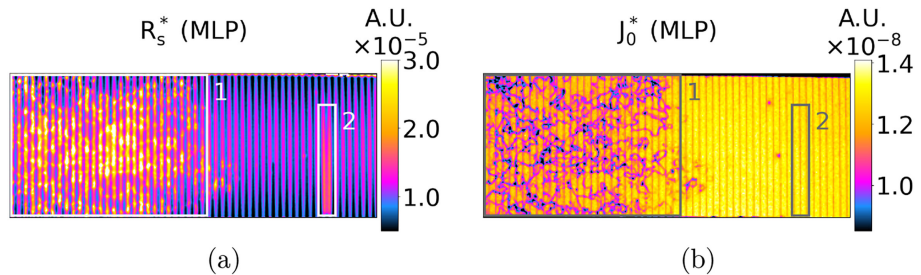


FIGURE 2 | (a) R_s^* and (b) J_0^* maps predicted with two independent MLPs corresponding to the area of Figure 1b inside the red rectangle. The regions marked “1” and “2” in the figures indicate, respectively, an area with high dislocation concentration and a damaged finger. [Color figure can be viewed at wileyonlinelibrary.com]

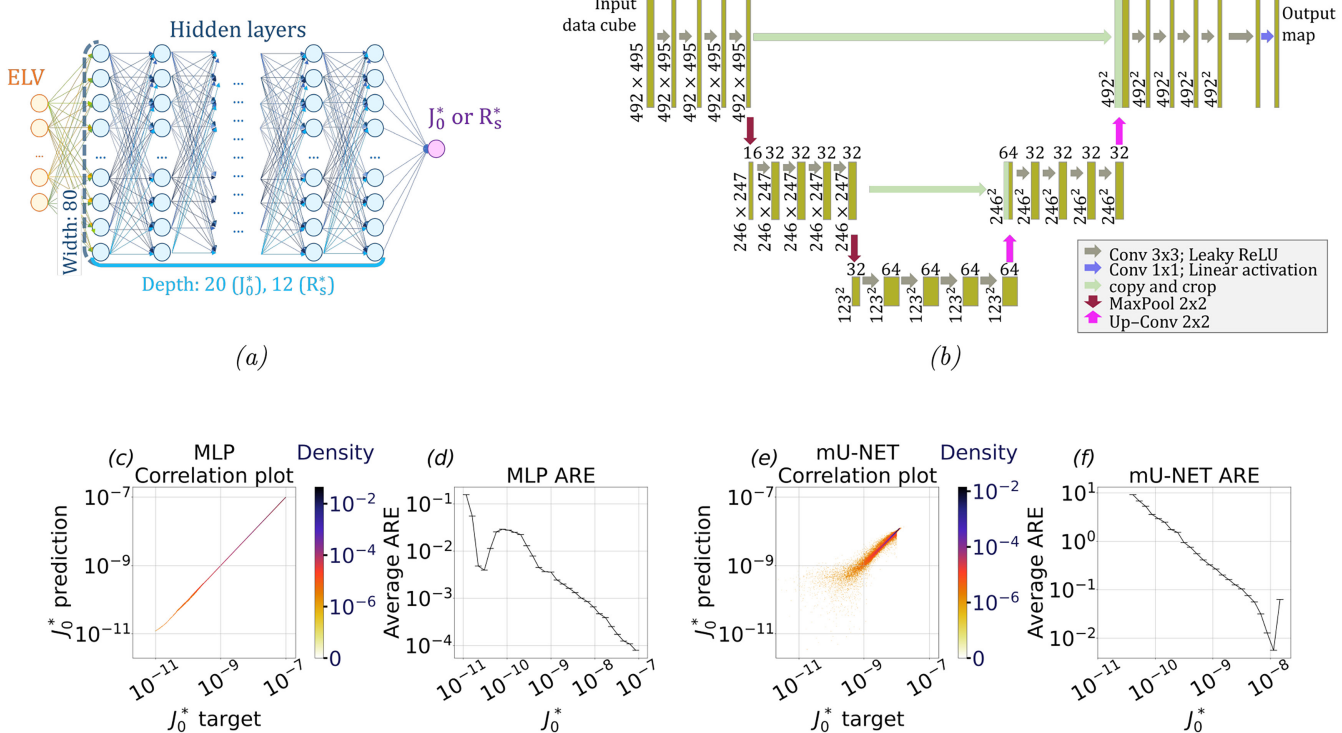


FIGURE 3 | (a) Representation of the multilayer perceptron (MLP) utilized for a pixel-wise prediction of R_s^* and J_0^* . (b) Modified U-NET (mU-NET) architecture used for R_s^* prediction, the last layer is followed by a linear activation function because the NN is used for regression. Comparison of the MLP (c) and mU-NET (e) J_0^* predictions to the targets of the synthetic test dataset (simulated without noise). The corresponding coefficients of determination are $1 - R_{test}^2 = 7.8 \times 10^{-8}$ for the MLP and $1 - R_{test}^2 = 8.8 \times 10^{-3}$ for mU-NET. ARE of MLP (d) and mU-NET (f) J_0^* predictions averaged over small intervals in \log_{10} scale of the test dataset. [Color figure can be viewed at wileyonlinelibrary.com]

a high R_s^* but are not distinguishable on the J_0^* maps contrary to the dislocations; see Region 2 in Figure 2a,b. This highlights the difference between recombination (J_0^*) and carrier transport (R_s^*) quality. Moreover, R_s^* is noticeably smaller near the busbars, particularly on the right side of Figure 2a, where no dislocations are present. This is because this pseudoparameter incorporates injection effects.

2.2 | ML Models and Their Accuracy

2.2.1 | Results on Synthetic Test Dataset

Two deep learning models are compared in this study: the first one is a MLP, and the second one is a CNN, a mU-NET. The architectures of those NNs are presented in Figure 3a,b, discussed

in Section 5.3, and the detailed hyperparameters are presented in Tables S1 and S2.

The MLP performs a pixel-wise analysis of the data, it takes an ELV vector corresponding to one single spatial pixel as input. It is a feedforward NN, the data flow from the input, corresponding to ELV in Figure 3a, through the hidden layers, represented in blue in Figure 3a, to the network's output, R_s^* or J_0^* in this case. The MLP is a fully connected architecture: each node is connected to every neuron in the directly preceding and following layers. It can process and output 1D data type and is able to approximate nonlinear functions, as demonstrated by the universal approximation theorem [37–39].

The CNNs, on the other hand, process the entire data cube at once, and consequently both deal with spatial features and with the third dimension of the data cube, here the voltage bias. CNNs ordinarily outperform other types of NNs in processing image and audio signal inputs, they play an essential role in computer vision. CNNs operate by using localized receptive fields and demonstrate strong performance in feature detection thanks to the training of various filters that identify distinct patterns. UNET, a specialized type of CNN originally developed for medical image segmentation, incorporates a contracting path for feature detection, similar to the one represented on the left side of Figure 3b, and a symmetric expanding path to preserve the input image's resolution, analogous to the one depicted on the right side of Figure 3b. The CNNs used in this study, mU-NETs, are adapted for regression purposes.

As there are two different parameters to extract from the data, namely, J_0^* and R_s^* , two different networks for each ML method are trained on synthetic datasets generated without noise, as described in Section 5.3. For the sake of simplicity, only the results maps for J_0^* will be depicted in the main text, the ones for R_s^* will refer to the supplementary information.

The first step is to assess the intrinsic quality of the networks by comparing the predictions with the test targets; see Figure 3c–f for J_0^* and Figure S1a–d for R_s^* . The corresponding coefficients of determination R^2 allow to globally evaluate the learning quality: They are greater than 0.98 for all four networks. For the MLPs, both R^2 are very close to 1 ($1 - R_{(R_s^*)}^2 = 6.8 \times 10^{-7}$ and $1 - R_{(J_0^*)}^2 = 7.8 \times 10^{-8}$), and the prediction versus targets graphs, presented in Figures 3c and S1a, show a quasistraight correspondence. For the mU-NETs, the R^2 coefficients are lower ($1 - R_{(R_s^*)}^2 = 1.2 \times 10^{-2}$ and $1 - R_{(J_0^*)}^2 = 8.8 \times 10^{-3}$), and the two prediction versus targets graphs, represented in Figures 3e and S1c, are more scattered, especially around the lowest values. Nevertheless, the predicting ability of the mU-NETs is noticeable.

R_s^* and J_0^* values extend over several orders of magnitude in the test datasets (and likewise in the training datasets). To assess the predicting capacity per order of magnitude, the average absolute relative error (ARE) is computed per small ranges in \log_{10} scale according to the following formula:

$$ARE = \left| \frac{y_{pred} - y_{ref}}{y_{ref}} \right|. \quad (3)$$

The evolution of the ARE as a function of the target values is respectively illustrated in Figure 3d,f for the MLP and mU-NET predicting J_0^* and in Figure S1b,d for the MLP and mU-NET predicting R_s^* . For two MLPs, the ARE decreases as the target values increase, except at very low values where the behavior is not monotonic. This can be attributed to the density of training data, which is higher for greater orders of magnitude. In the lower range of the training intervals, the density of data points is very low and that can account for the deviation of the ARE from the general trend observed. For the mU-NET network predicting J_0^* , the ARE decreases to values below 1% for J_0^* values around 10^{-8} and then slightly increases for larger values. The peak of the J_0^* distribution in the mU-NET training data is around 10^{-8} , which may explain this observation. For the mU-NET network predicting R_s^* , the ARE decreases until 10^{-5} and oscillates for larger values.

In summary, all ML models are able to learn correctly how to map synthetic and noise-free ELV inputs to R_s^* or J_0^* values. Remarkably high coefficients of determination are obtained for the test datasets. The evolution of the test ARE as a function of the target order of magnitude indicates that the learning quality is particularly high for the largest target values.

2.2.2 | Comparison of ML Predictions With NLLS Fitting Results

After having evaluated the prediction performance of the ML models using synthetic data, we perform an analysis based on experimental data. To do this, we compare the ML outputs with the ones obtained by NLLS fitting on EL images measured on an Al-BSF silicon solar cell with high dislocation content areas as depicted in Figure 1b. The characteristics of these data are described in Section 5.2. The method employed for NLLS fitting is detailed in Section S2.2.

The maps of the parameters R_s^* and J_0^* predicted with the MLPs are presented in Figure 2, and the ones predicted with mU-NETs and the reference corresponding to the NLLS predicted maps are presented in Figure S2. We study their difference using two indicators: the ARE between the ML predictions and the reference and the structural dissimilarity index (D-SSIM) defined as

$$D\text{-SSIM} = 100 - SSIM(\%). \quad (4)$$

The structural similarity index (SSIM) was introduced by [40] in 2004; it assesses the perceived quality of an image in comparison to a reference. We chose to use D-SSIM instead of SSIM to highlight differences rather than similarities between the maps. Because the images we compare are highly similar, even a slight improvement in SSIM, for example, from 99% to 99.5%, results in a significant reduction in D-SSIM, which would be halved in that scenario. The SSIM integrates a luminance comparison function, a contrast comparison function, and a structure comparison function. By default, these three functions are weighted equally in the SSIM computation. The indicator is locally computed within a window, applying a circular-symmetric Gaussian filter for weighting the values. Detailed computation methods are described in Section S2.5. This filter is sized at 10×10 in our case. Indeed, in the studied cells maps, the distance between two fingers is of the order of

5 pixels, the area separating a finger from its two neighbors is then of 10 pixels approximately. This is taken as the characteristic distance to compute the D-SSIM and justifies the choice of the filter size.

Maps of ARE and D-SSIM comparing ML predictions with NLLS fitting results are presented in Figure 4 for J_0^* and Figure S3 for R_s^* . The average ARE and D-SSIM values are calculated for the two subareas delimited in these figures by the blue rectangle (left, dislocation area) and green rectangle (right, no visible dislocations) which are part of the larger one previously outlined by the red perimeter in Figure 1b. The values are reported in Tables 1 and 2.

A pixel-wise comparison between NLLS and the MLP is first performed using ARE, as shown in Figures 4a,b and S3a,b. ARE is lower in damaged areas (broken finger and dislocations zone) for both the MLP and the mU-NET predictions of J_0^* (cf. Figure 4a,b and Table 1). This result is expected for mU-NET predictions, because J_0^* values are closer to 10^{-8} on dislocations than on defect-free areas (see Figure 2) and that the minimum of ARE is obtained for 10^{-8} for the test dataset. However, this is unexpected for the MLP. As shown in Figure 3d, lower AREs were

expected for higher J_0^* values. This discrepancy in the networks' behavior when processing synthetic data and experimental data may arise from experimental noise. To test this hypothesis, we examined the ARE for J_0^* after predictions on synthetic data with and without added noise. Figure S4 illustrates the evolution of the ARE for MLP-predicted J_0^* values as a function of the R_s^* and J_0^* values. In Figure S4a, the MLP input data are synthetic and generated without noise; we see that the ARE is mainly influenced by the J_0^* value. In contrast, Figure S4b shows that when noise is introduced to the input data, the resulting ARE is influenced by both R_s^* and J_0^* . This demonstrates how noise impacts the MLP behavior. ARE on the MLP predictions of R_s^* is slightly lower on the areas corresponding to dislocations (cf. Figure S3a and Table 1). In that case, this is consistent with the observation that ARE is lower for higher values of R_s^* in the test synthetic dataset, as shown in Figure S1b. ARE on the R_s^* mU-NET predictions is fluctuating between low and high values on the dislocation area.

More generally, observations on ARE can also be explained by the fact that, on defective areas, EL intensity is smaller and increases more slowly with voltage than on defect-free areas. Consequently, the intrinsic variance of the ELV curve decreases

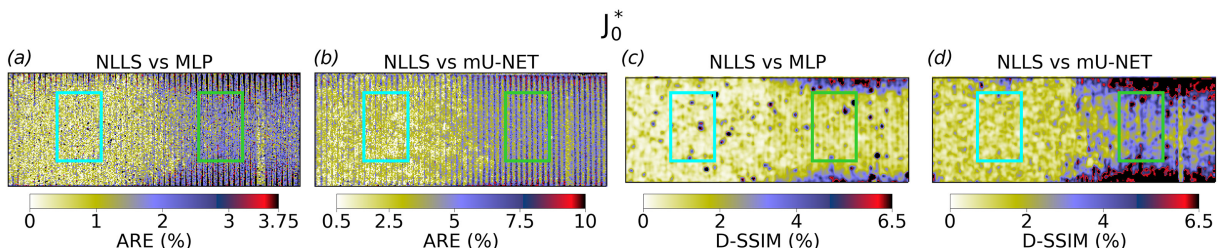


FIGURE 4 | Absolute relative error (ARE) between the J_0^* reference prediction (NLLS fit) and the MLP (a) or mU-NET predictions (b). Structural dissimilarity index (D-SSIM) maps comparing the reference predictions and the MLP (c) or mU-NET (d) predictions. The average ARE and D-SSIM values in the blue (left, dislocation area) and green (right, no visible dislocations) rectangles are presented in Tables 1 and 2. The region represented in these figures corresponds to the one delimited by the red rectangle in Figure 1b. [Color figure can be viewed at wileyonlinelibrary.com]

TABLE 1 | ARE (%) averaged on the two areas delimited by the blue (left) and green (right) rectangles in Figures 4a,b and S3a,b, calculated with NLLS maps as references.

	ARE (%)			
	R_s^*		J_0^*	
	With dislocations	Without dislocation	With dislocations	Without dislocation
MLP	1.1	1.4	0.9	1.9
mU-NET	11.0	13.5	2.6	4.9

TABLE 2 | Structural dissimilarity indices (D-SSIMs) averaged on the two areas delimited by the blue (left) and green (right) rectangles in Figures 4c,d and S3c,d, calculated with NLLS maps as references.

	D-SSIM (%)			
	R_s^*		J_0^*	
	With dislocations	Without dislocation	With dislocations	Without dislocation
MLP	0.04	0.08	0.82	1.33
mU-NET	16.43	1.62	1.13	3.40

and this may make the low-intensity curves more robust to noise during regression. Moreover, in regions with defects, R_s^* is higher, and the curvature (second derivative) of the ELV at high voltage is consequently more pronounced, which facilitates the estimation of R_s^* .

There is also a visible similarity between all the maps resulting from the different networks' predictions. Beyond visual assessment, we compute the D-SSIM between the maps resulting from NLLS fitting and MLP predictions, as presented in Figures 4c and S3c, or mU-NET predictions, as shown in Figures 4d and S3d. As for ARE, the average D-SSIM values on a dislocation and a dislocation-free area (rectangles, respectively, at left and right sides of the maps) are shown in Table 2. All average D-SSIM values are very low, except for the mU-NET-based R_s^* predictions on the dislocation area.

Conclusions for J_0^* predictions are the same than with ARE maps: the dissimilarity is lower on the left side of the maps, corresponding to dislocation areas. A similar observation can be done for the MLP-predicted R_s^* map. However, for the mU-NET predicted R_s^* map, the D-SSIM is much higher on the areas corresponding to dislocations than on the areas corresponding to

higher EL intensities. The R_s^* and J_0^* values vary very rapidly on those dislocation areas, if the up-sampling part of the mU-NET network is not well trained, it may lead to an inability to restore such strong variations of intensity in the output. This might explain the larger D-SSIM values for the map comparing the R_s^* NLLS fitted and mU-NET predicted values, and this could also account for the highest error values on ARE map for the mU-NET predicted R_s^* .

On average, the mU-NET predictions show greater deviation from the NLLS predictions compared to the MLP predictions. The mU-NET model trained for J_0^* is yet very accurate, with an ARE around 7% for the areas with the highest error on Figure 4b. The mU-NET model trained for R_s^* prediction is, in contrast, much less accurate, with an ARE reaching values greater than 25% in the dislocation area. R_s^* being proportional to the series resistance R_s , the choice of using or not the mU-NET model for the R_s^* prediction depends on the needed precision on R_s .

Furthermore, we observe that the ML predictions are generally closer to the NLLS fitting results on the dislocation areas, and also on the damaged finger area for the J_0^* predictions. This

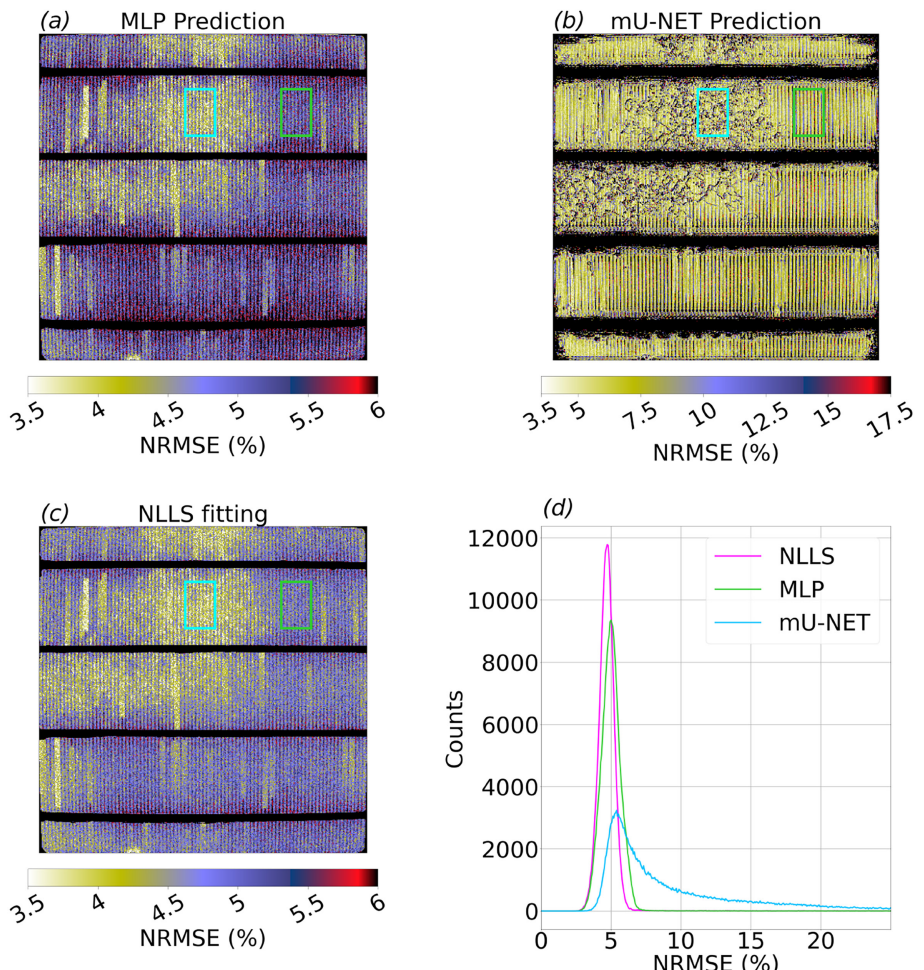


FIGURE 5 | Normalized root mean square error (NRMSE) comparing for each spatial pixel the experimental ELV measurements to the fitted ELV curves generated using the MLP (a), mU-NET (b), or NLLS (c) R_s^* and J_0^* predicted values. The blue (left) and green (right) rectangles correspond to the same areas with and without visible dislocations as in Figure 4, and the average NRMSE values in those areas are shown in Table 3. Histogram (d) showing the NRMSE distribution after ML or NLLS prediction of the R_s^* and J_0^* maps. [Color figure can be viewed at wileyonlinelibrary.com]

suggests the possibility of very accurate analyses of defects on the solar cells with the ML models.

2.3 | ML Methods as Standalone Regression Tools

Previous analyses have shown the ability of the models to reproduce already known data from NLLS calculations. Hereafter, we will study the intrinsic performance of the models as self-sufficient regression tools for physical parameter extraction.

The ML prediction error estimation based on the comparison with NLLS fitting results allows for the separation of the error on R_s^* from the error on J_0^* . Nonetheless, because the ultimate goal is to replace NLLS fitting with ML-based regression methods, this approach is not optimal. The computation of the normalized root mean square error (NRMSE), an estimator of the prediction error that depends on both R_s^* and J_0^* , permits the rapid generation of an error map following the ELV analysis:

$$NRMSE = \sqrt{\frac{\sum_{V_i} \left[EL_{pred}(J_{0,pred}^*, R_{s,pred}^*, V_i) - EL_{exp}(V_i) \right]^2}{\sum_{V_i} [EL_{exp}(V_i)]^2}}. \quad (5)$$

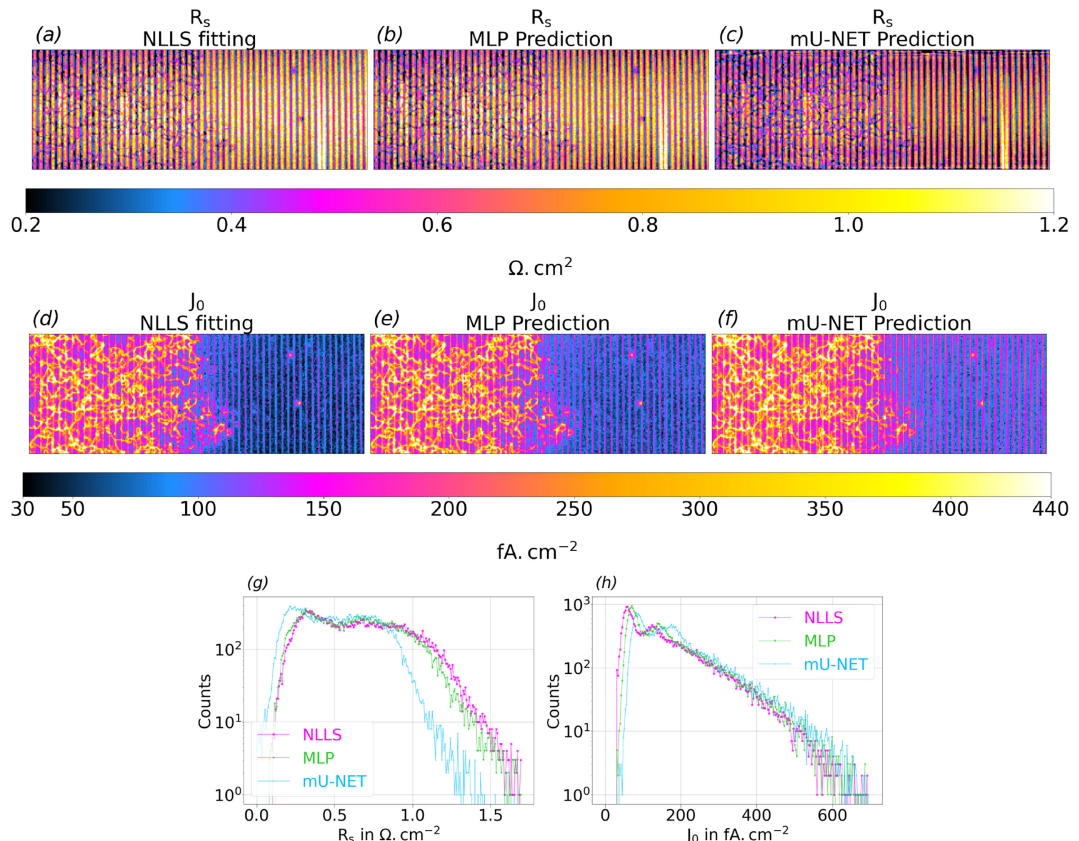


FIGURE 6 | Series resistance R_s ($\Omega \cdot \text{cm}^2$) and dark saturation current J_0 ($fA \cdot \text{cm}^{-2}$) maps based on the NLLS (respectively, a and d), the MLP (respectively, b and e) and the mU-NET (respectively, c and f) predictions of the pseudoparameters R_s^* and J_0^* (see Figures 2 and S2). Distribution of the R_s (g) and J_0 (h) values predicted using the three methods and corresponding to the maps, respectively, (a) to (c) and (d) to (f). [Color figure can be viewed at wileyonlinelibrary.com]

Figure 5 shows NRMSE maps based on the MLP (a), the mU-NET (b), and the NLLS (c) predictions corresponding to an entire cell analysis; the cell is the same as in Figure 1b. The average value of the NRMSE on areas with (blue, left rectangle) and without (green, right rectangle) visible dislocations are summarized in Table 3. Those areas match the ones delimited by the two rectangles in Figure 4.

We observe that both NLLS and MLP demonstrate superior performance in predicting the pseudoparameters on areas corresponding to dislocations and to damaged fingers than on the other parts of the cells. This corroborates the previous observation that very accurate analyses of the defects are possible with at least MLP and NLLS. In contrast, NRMSE is higher on

TABLE 3 | NRMSE averaged on the two areas delimited by the blue (left, with dislocations) and green (right, without visible dislocation) rectangles in Figure 5a–c.

	NRMSE(%)	
	With dislocations	Without dislocation
NLLS	4.2	4.8
MLP	4.2	5.1
mU-NET	9.1	8.0

dislocation areas for the mU-NET. This can be explained by the fact that the error on R_s^* influences the high ELV values and weights more in the NRMSE computation. Indeed, R_s^* has an influence at high voltage (high EL intensity) whereas J_0^* has an influence at lower voltage (lower EL intensity).

Figure 5d shows the distributions of NRMSE arising from the utilization of the three methods and not relevant data corresponding to the busbars are removed before computing them. The NRMSE distribution resulting from the MLP prediction (mode at 5.0%, median at 5.04%) is very close to the one resulting from the NLLS fit (mode at 4.7%, median at 4.74%). The one resulting from the CNN prediction is more flattened and centered towards higher values (mode at 5.4%, median at 7.81%) but stays low.

We tested our ML models on seven other solar cells with a varying dislocation concentration for further evaluation. The distribution of NRMSE subsequent to the use of the different methods is shown in Figure S5. The cell studied above corresponds to the seventh sample. The conclusion drawn for this last are the same than the ones arising from the other samples study: the NLLS method is the most accurate, the MLP provides very similar results, and the mU-NET leads to a higher error on average, but it can be precise enough depending on the requirements of the characterization.

2.4 | Computation of R_s and J_0

In this section, making use of the theory of [22] and summarized in Section 5.1, we finally compare the physical parameters R_s and J_0 derived from R_s^* and J_0^* obtained with ML methods to those obtained via NLLS. This will give a pragmatic statement on ML methods. A comparison of the R_s and J_0 predictions based on the ELV model (Equation 1) with other EL-based estimations [41, 42] of these parameters was conducted in [22], demonstrating the reliability of this model.

Figure 6a-f shows the R_s and J_0 maps computed using the regression results of the three methods. They are all very similar, and the corresponding parameter distributions depicted in Figure 6g,h are also very analogous. One can however notice from the distributions that the use of mU-NET leads to a small underestimation of the R_s values. The computation of the average D-SSIMs (see Table 4) permits to compare the R_s and J_0 maps obtained from ML predictions of pseudoparameters with those from NLLS fitting, confirming the proximity between different maps. As the MLP-predicted pseudoparameters are closer to the NLLS results than the mU-NET ones, the D-SSIMs comparing the parameters derived from the MLP predictions with those from the NLLS fitting are also lower than for mU-NET.

Overall, despite of the errors on the pseudoparameter predictions, the two ML-based regression methods lead to predictions of parameters J_0 and R_s that are very close to the ones predicted using the NLLS fitting technique.

2.4.1 | Computation Time

Table 5 compares the prediction time of all three methods. It is dramatically reduced with ML. Indeed, for a 250,000-pixel data

TABLE 4 | D-SSIM comparing the R_s and J_0 maps resulting from the ML predictions of the pseudoparameters to the ones resulting from NLLS fitting.

D-SSIM (%)	R_s	J_0
MLP	1.0	1.9
mU-NET	8.3	7.4

TABLE 5 | Duration of the analysis of a 250,000-pixel silicon solar cell ELV imaging on a computer with a processor Intel Core i7-11850H.

	Nonlinear least squares	MLP	mU-NET
Prediction time	≈1 h	≈15 s	≈3 s

cube, 3s are necessary to predict both the R_s^* and the J_0^* maps with mU-NET (the analysis duration is divided by 1200 compared to NLLS), and the prediction of these same maps using the MLP takes 15s (the analysis duration is divided by 240 compared to NLLS).

Both networks perform well and present distinct advantages: The mU-NET is faster but is less accurate than the MLP. The precision difference is especially remarkable in the areas corresponding to dislocations, where the mU-NET NRMSE averages more than twice that of both the MLP and the NLLS NRMSE (9.1% vs. 4.2%). This contrast is much less important on parts of the cells without defects: The average NRMSE is there equal to 5.1% using the MLP and to 8.0% using mU-NET; see Table 3. One may choose the CNN if the computation time must be short, and one may choose the MLP if the precision is the priority.

The ML models are trained to be used many times, and in that case, the training duration (presented in Section 5.3.3) is counterbalanced by the time saved during data analysis. The proposed method is relevant for industrial purposes (such as systematic end-of-line analysis) where the studied cells correspond to the same architecture and can consequently be represented by a single and relatively small training dataset. It is also relevant for research purposes, if a lot of cells with similar electro-optic properties need to be studied in a short amount time or for aging studies where a large number of measurements are repeatedly performed on the same cells. The more diverse are the samples to analyze, the larger is the corresponding training dataset and generally the longer is the training time [30] or the greater are the parallel resources to use [43].

3 | Perspectives

3.1 | How Far to Optimize? Balancing Accuracy and Analysis Duration

The three approaches used to fit ELV data cubes rely on optimization algorithms. NLLS involves for each pixel the minimization of the MSE:

$$MSE = \frac{\sum_{i=1}^N [EL^{exp}(V_i) - EL^{fit}(V_i)]^2}{N}, \quad (6)$$

to find the optimal pair $\{R_s^*, J_0^*\}$. Likewise, during the training phase, the supervised ML algorithms perform minimization of loss functions comparing the ML output values to the target values in order to find an optimal set of weights and biases.

In the three cases, the noise on experimental data limits the precision of the regression. Indeed, in NLLS fitting, the noise causes the measurements to deviate from the physical model (Equation 1). This leads to an uncertainty on the fitted parameters in the best scenario and to several possible solutions (local minima) in the worst scenario. The ML models are trained on synthetic data generated using Equation (1) and without addition of noise. They can learn the physical model with an arbitrary low precision, but when dealing with experimental measurements, the noise will limit the precision of their prediction.

To corroborate this reasoning, the average evolution of the tolerance for termination of NLLS optimization is compared with the average evolution of NRMSE resulting from each fitting iteration in Figure 7a. Similarly, Figure 7b shows the average NRMSE (left axis) and the interquartile range (right axis) resulting from the MLP predictions of R_s^* and J_0^* , using the networks weights saved after each epoch for each of the two models. The average is computed on a set of 400 experimental ELV curves for the NLLS fitting and on the ELV data cube corresponding to Figure 1b (without the busbars) for the MLP predictions.

The utilized NLLS minimization function is the *least_squares* function of the *scipy.optimize* Python library [44]. In this function, four parameters can determine when the optimization stops: the tolerance for termination “by the change of the variable” x_{tol} , “by the norm of the gradient” g_{tol} , “by the change of the cost function” f_{tol} and the “maximum number of function evaluations before the termination” max_{nfev} [45]. As explained in the function documentation, the optimization process ends when either $norm(dx) < x_{tol} \times (x_{tol} + norm(x))$ with x the variables

vector, or $norm(g_scaled, ord = np.inf) < g_{tol}$ with g_scaled the gradient scaled to account for the presence of the bounds, or $dF < f_{tol} \times F$ with F the cost function, or when $niter > max_{nfev}$ with $niter$ the number of iterations. In this study, the relevant tolerance parameter is x_{tol} , as it is observed to be the first tolerance criterion to be reached in most cases.

In Figure 7a, the average value of $x_{tol}^{compare} = norm(dx)/(x_{tol} + norm(x))$ decreases as the number of optimization iterations increases. However, the average NRMSE value and the corresponding interquartile range cease to decrease around the 40th iteration. It means that even though during the optimization process the variation of the variable vector $[R_s^*, J_0^*]$, from one iteration to the next, decreases until reaching very low values, it is not relevant to wait such thing to stop the fit. When the NRMSE stabilizes, it can be considered that the fitting precision is sufficient. A new condition to stop the optimization, based on a NRMSE threshold (which has the interest of being normalized), could be implemented to limit the fitting time. This would be possible in the case of this study because we have a knowledge of the noise level in the experimental data.

In Figure 7b, the average NRMSE ceases to decrease around the 70th training iteration whereas the training loss keeps decreasing until the last iteration for both MLPs (predicting R_s^* and J_0^*) as shown in Figure S6. It means that after the 70th training iteration, noise appears to dominate the discrepancy between the experimental data and the ELV generated using the physical model. Considering the NRMSE indicator, the second half of the training process could be deemed dispensable and the training time could be reduced by half in that case.

To summarize, studying error indicators such as the NRMSE, that are both sensitive to the fitting quality and to the noise, allows to propose new optimization thresholds to reduce the number of iterations without affecting the final regression error.

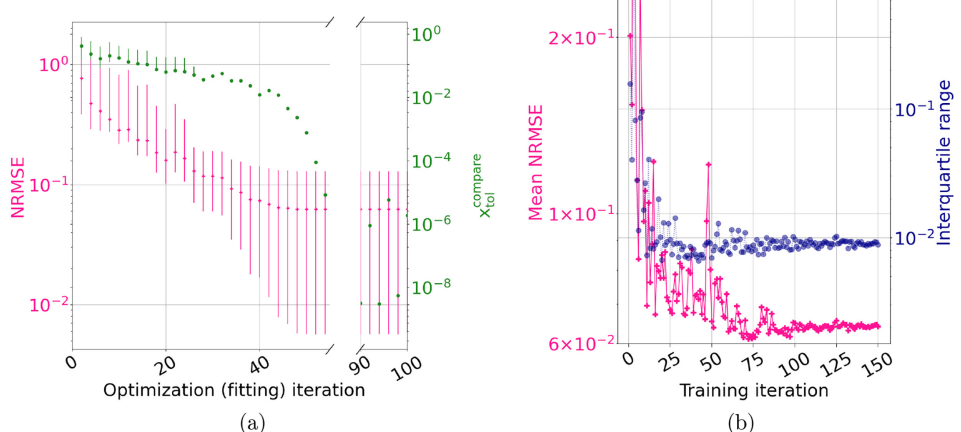


FIGURE 7 | (a) Evolution of the average value and interquartile range of the NRMSE (left axis) and of $x_{tol}^{compare}$ stopping criterion (right axis) after an increasing number of optimization iterations performed by the NLLS fitting algorithm on 400 ELV inputs. (b) Evolution of the average NRMSE (left axis) and of the interquartile range (right axis) computed after prediction of J_0^* and R_s^* based on experimental data (a solar cell ELV data cube without the busbars) for each training iterating of MLPs. [Color figure can be viewed at wileyonlinelibrary.com]

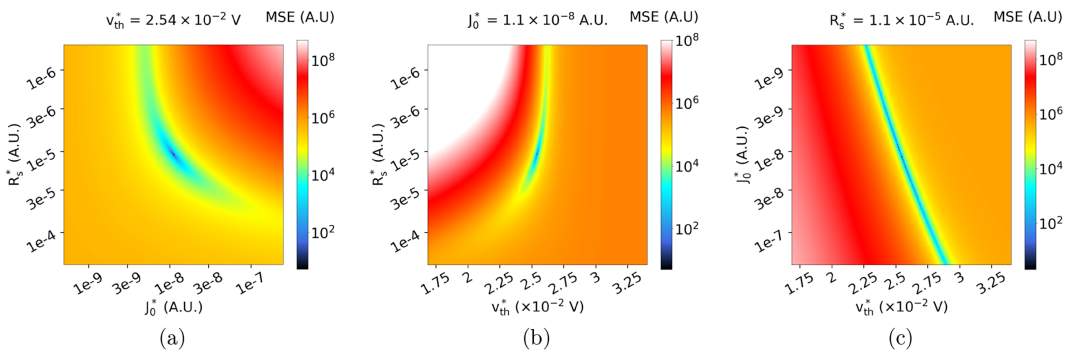


FIGURE 8 | MSE between ELV_{ref} , computed for $R_s^* = 1.1 \times 10^{-5}$, $J_0^* = 1.1 \times 10^{-8}$, and $v_{th}^* = 2.54 \times 10^{-2}$ V (corresponding to $T = 295$ K), and (a) ELV computed at $v_{th}^* = 2.54 \times 10^{-2}$ V for varying values of R_s^* and J_0^* ; (b) ELV computed at $J_0^* = 1.1 \times 10^{-8}$ for varying values of R_s^* and v_{th}^* ; and (c) ELV computed at $R_s^* = 1.1 \times 10^{-5}$ for varying values of J_0^* and v_{th}^* . [Color figure can be viewed at wileyonlinelibrary.com]

3.2 | Performance of the Physical Model: The Effect of the Pseudothermal Voltage

So far, we have addressed a two-variable problem. We will first confirm the uniqueness of the solution $\{R_s^*, J_0^*\}$ when the pseudothermal voltage v_{th}^* is fixed and then introduce v_{th}^* as a third variable into the fitting procedure. Indeed, a low fitting error, such as the small NRMSE obtained when fitting ELV data, does not demonstrate the uniqueness of the regression solution, a requirement for ensuring the physical relevance of the fitting result.

We studied crystalline silicon solar cells with regulated temperature during measurements. Given silicon's high thermal conductivity, it is reasonable to assume that the temperature is uniform across the cell. Yet, in some cells, local temperature variations may occur due to the presence of defects. Accordingly, the pseudothermal voltage may be an undetermined variable of the system, and one might be tempted to fit the three variables R_s^* , J_0^* , and v_{th}^* .

Figure 8a shows the MSE between a noise-free reference ELV curve ELV_{ref} and ELV vectors computed for a large range of R_s^* and J_0^* values with a fixed v_{th}^* . ELV_{ref} is computed for J_0^* and R_s^* values corresponding to the ones typically observed in our study, namely, $J_0^* = 1.1 \times 10^{-8}$ and $R_s^* = 1.1 \times 10^{-5}$. The pseudothermal voltage v_{th}^* used to compute ELV_{ref} corresponds to a temperature $T = 295$ K, matching our typical experimental conditions. In Figure 8a, there is a single MSE minimum within the given parameter range of interest and, consequently, a unique solution $\{R_s^{*,opt}, J_0^{*,opt}\}$ to the NLLS minimization.

It is also possible to fit R_s^* if neither J_0^* nor v_{th}^* are known, as depicted in Figure 8a,b where a global minimum is reachable. However, it is not possible to find a unique combination of the three parameters for the ELV fit. As shown in Figure 8c, when fitting an ELV curve, a wide domain of $\{J_0^*, v_{th}^*\}$ pairs, visible as a blue line crossing the graph, permits to reach very low MSE values. The J_0^* values presented in this figure lie in the interval $I_{J_0^*}^1 = [5 \times 10^{-10}, 2.5 \times 10^{-7}]$, and almost all of them allow for fitting ELV_{ref} with a very low error. This amount of uncertainty is not physically acceptable. Indeed, this interval is greater than the range of values $I_{J_0^*}^2 = [0.8 \times 10^{-8}, 1.6 \times 10^{-8}]$ observed in a group of seven silicon solar cells, as shown in Figure S8, for which J_0^*

is computed at $T = 295$ K. The low MSE v_{th}^* values are distributed over a smaller range, approximately $[2.25, 3] \times 10^{-2}$ V.

There appears to be, at least computationally, a nonidentifiability of all the model parameters. Measurements of temperature during the luminescence collection is necessary for a correct estimation of J_0^* .

Let us mention that the impossibility to extract both the ideality factor n_{id} and the saturation current from one IV curve using the single-diode model has been observed in [4]. Because the ELV (Equation 1) model is built mimicking the dark single-diode IV model and that the pseudosaturation current J_0^* and v_{th}^* , respectively, hold the same position as the saturation current and n_{id} in the single-diode model, one can infer that the work reported in [4] meet the same nonidentifiability problem as we do. In [46, 47], figures similar to Figure 8c are shown, but the variables of interest are the saturation current J_0 and the ideality factor n_{id} instead of J_0^* and v_{th}^* . Large domains $\{J_0, n_{id}\}$ that permit fitting an IV curve with a low error are also depicted. The authors of [47], however, focus on the low MSE of their results, which they consider reliable enough, while neglecting the observable existence of multiple solutions. In [46], the authors compensate the existence of this low MSE $\{J_0, n_{id}\}$ domain by introducing a fixed relationship between R_s and n_{id} that constrains the possible solutions. This relationship is obtained by derivation of the voltage with respect to the current around the open-circuit voltage point (zero current). However, this solution is not directly transferable to our case because the signal at low EL intensity is very noisy; its numerical derivative would probably not be reliable.

4 | Conclusion

We demonstrated that two ML models of interest, the MLP and the mU-NET, are able to inverse the physical model describing the ELV phenomenon in silicon solar cells with significantly good accuracy. Both are able to predict reliable values of the pseudoparameters R_s^* and J_0^* with standardized errors ranging from 5% to 8%. The MLP is the most accurate of the two, achieving fitting precision similar to NLLS. ML models permit the processing of data cubes much faster than when using NLLS, reducing the analysis duration by a factor of 100–1000, with mU-NET being the fastest method. The selection of the NN depends

on prioritizing either the reduction of data processing duration or prediction precision.

We also showed that the estimations of the optoelectronic parameters R_s and J_0 derived from the ML-predicted pseudoparameters were reliable. The distributions of these parameters obtained using different methods were very similar and the D-SSIM comparing the ML-derived estimations to those obtained via NLLS did not exceed 10%.

These results pave the way for real-time analysis of solar cells and for precise analysis of modules. A data cube resulting of measurements on a 72 cells module, with the same resolution as in this paper, would contain approximately 18×10^6 spatial pixels. Using the NLLS method to process this data would require 3 days. Even if parallelizing the computation could allow to save a large amount of time, the analysis would still take several hours. With the mU-NET models or the MLP, respectively, only 4 or 18 min would be necessary to process this volume of data and further computation optimization might reduce this duration.

The proposed method can be propagated to the analysis of other kinds of data cubes, such as PL hyperspectral imaging cubes, assuming a physical model exists to describe the phenomena of interest. We employed several techniques to quantify the prediction error: ARE and D-SSIM necessitating the knowledge of a reference and the NRMSE directly assessing how close the result of the regression is to the input data. We also demonstrated the importance of mapping the fitting error around typical parameter values to ensure the uniqueness of the regression results.

5 | Methods

5.1 | Derivation of R_s and J_0 From R_s^* and J_0^*

The local voltage-dependent EL emitted by a silicon solar cell can be written as [22]

$$EL(V_T, E, r) = EQE(E, r) \varphi_{BB}(E, T) \exp \left[\frac{V_T - R_s^*(r) EL(V_T, E, r)}{v_{th}^*} \right]. \quad (7)$$

v_{th}^* is defined in Equation (2). $EQE(E, r)$ is the external quantum efficiency of the cell, function of the position r and of the energy E . $\varphi_{BB}(E, T)$ is the black-body emission.

A calibration matrix K_{cal} allows to compute the photon flux striking the camera sensor:

$$K_{cal} = \frac{\pi T_R T_{opt} \cos^4(\theta) S_{pixel} t_{acq}}{G \times 4N^2 (1 + |g_y|^2)}, \quad (8)$$

with G the conversion factor of the camera, T_R the transmittance of the ambient atmosphere, T_{opt} the transmittance of the optical system, N the f -number of the objective, g_y is the transverse magnification, t_{acq} the acquisition time, S_{pixel} the pixels surface, and θ the angle between the optical axis and the direction from the center of the objective to the solar cell pixel.

Furthermore, the flux, modulated by the quantum efficiency of the camera QE_{cam} , is integrated over photon energies. The EL signal recorded by the camera is subsequently:

$$EL_{cam}(r, V_T) = K_{cal} \times \exp \left[\frac{V_T - R_s^*(r) EL_{cam}(V_T, E, r)}{v_{th}^*} \right] \int EQE(E, r) \varphi_{BB}(E, T) QE_{cam}(E) dE. \quad (9)$$

In the following and in the other sections of the paper, we simplify the notation EL_{cam} by the notation EL . J_0^* is defined as

$$J_0^* = K_{cal} \int EQE(E, r) \varphi_{BB}(E, T) QE_{cam}(E) dE. \quad (10)$$

The EQE depends on the effective diffusion length L_{eff} :

$$EQE(E) = \frac{1 - R(E)}{1 + \frac{\cos(\beta)}{\alpha L_{eff}}}, \quad (11)$$

with β the average path angle of the photons with respect to the cell's normal vector, $R(E)$ the reflectivity losses, and α the absorption coefficient of silicon. Accordingly, the value of L_{eff} can be deduced from J_0^* and the dark saturation current J_0 can then be computed:

$$J_0 = q \frac{n_i^2}{N_A} \frac{D}{L_{eff}}, \quad (12)$$

with n_i the intrinsic carrier concentration, N_A the acceptor density, and D the diffusion coefficient.

The local voltage is $V(r) = V_T - R_s^* \times EL = V_T - \Delta V(r)$ with

$$\Delta V(r) = R_s(r) \left(J_0(r) e^{\frac{V(r)}{v_{th}}} + \frac{V(r)}{R_{sh}} \right). \quad (13)$$

We deduce that

$$R_s(r) = \frac{R_s^*(r) \frac{J_0^*(r)}{J_0(r)}}{1 + \frac{v_{th} \times J_0^*(r)}{J_0(r) \times EL(r, V_T) \times R_{sh}} \ln \left(\frac{EL(r, V_T)}{J_0^*(r)} \right)}, \quad (14)$$

if the shunt resistance R_{sh} is sufficiently large, as it the case for cell studied in this manuscript (see Section S2.1 and Figure S7), the second term in the denominator can be neglected. Then,

$$R_s(r) = R_s^*(r) \frac{J_0^*(r)}{J_0(r)}. \quad (15)$$

5.2 | Experimental Data

5.2.1 | ELV Measurements

The studied cells are Al-BSF solar cells built with silicon wafers extracted from mono-like silicon ingots. An increasing voltage bias, from 420 to 690 mV, is applied to the cells, and an EL image is

taken at each 10-mV step. The ELV measurements are performed using silicon sCMOS sensor-based camera ORCA Flash v2+ from Hamamatsu. The raw measurements are of size 2048×2048 pixels with a resolution of $90\text{ }\mu\text{m}$ per pixel. The temperature of the cells during measurements under consideration is of 295K. The temperature is regulated through copper plate with circulating water and controlled with a pyrometer (with a 0.95 emissivity). The experimental setup is identical to the one described in [22].

5.2.2 | Data Preprocessing

The ELV data cubes are processed before being analyzed.

The metallic contacts (busbars and fingers) do not emit luminescence, and assigning a J_0^* or R_s^* value to these areas of the cells is not meaningful. The EL signal in these regions is nonzero due to light diffusion and noise. While a mask is used to suppress the parasitic signal from the busbars, the fingers are too thin to apply the same treatment.

Subsequently to this, in order to reduce noise and accelerate computation, each EL images are resized at a 1/4 scale using bicubic interpolation. The *imresize* Matlab function is utilized. The resolution is consequently diminished and the resulting pixels correspond to $306 \times 306\text{ }\mu\text{m}^2$ squares.

Additionally, the dark offset map, incorporating all sources of noise, is computed by averaging the lowest voltage images before any EL signal is detectable. This is integrated into the fitting procedure.

In order to limit the number of operations performed on the input data cubes of the ML models, no smoothing or denoising of the data is applied. Our objective is to propose an algorithm performing well on noisy data. As a consequence, the fitting error or prediction error is expected to hit a threshold due to experimental noise.

Different normalization techniques have been tried, and the Z normalization

$$x_i^{norm} = \frac{x_i - mean(X)}{std(X)}, \quad (16)$$

with x_i a vector of the 2D (or 3D) dataset X composed of N (or $N_i \times N_j$) vectors, leads to the best results. For the MLPs, the input data are not normalized, and the output data are Z normalized with X corresponding to the training targets. For the mU-NETs, both the inputs and outputs are normalized with X corresponding to the training data (respectively, the ELV data cubes and the R_s^* or J_0^* maps).

5.3 | Deep NNs (DNNs)

5.3.1 | MLP

5.3.1.1 | Architecture of the MLP Models. To determine the optimal MLP architectures, balancing between training time and prediction accuracy, we employed a

trial-and-error approach. A width of 80 and a depth of 12 are used for the R_s^* network, and a width of 80 and a depth of 20 are used for the J_0^* network. The activation function is the rectified linear unit (ReLU), and the optimizer is Adam. The detailed training hyperparameters are presented in Table S1.

5.3.1.2 | Generation of the Synthetic Training Datasets. The MLP takes an ELV curve as input and predicts the corresponding R_s^* or J_0^* value. Two different networks are trained to predict independently the values of J_0^* and R_s^* .

We had at our disposal a set of data cubes corresponding to seven different silicon solar cells and the corresponding R_s^* and J_0^* maps resulting of NLLS fitting. The R_s^* and J_0^* distributions are plotted in Figure S8. A large number of $\{R_s^*, J_0^*\}$ pairs are generated using two independent random generators with uniform distributions including a majority of the NLLS estimated values on experimental measurements.

The training datasets leading to the lowest prediction error on experimental data are composed of 500,000 $\{R_s^*, J_0^*\}$ pairs with $R_s^* \in [10^{-7}, 10^{-3}]$ and $J_0^* \in [10^{-11}, 10^{-7}]$. Ten percent of the dataset is used as the validation dataset. A second dataset, the test dataset, of 25,000 input vectors and target pairs is generated likewise.

5.3.2 | CNN—mU-NET

5.3.2.1 | Architecture of the mU-NET Models. The architecture of the models is inspired from the U-NET network presented in [26]. Because the network is used for regression and not segmentation, the last activation layer is replaced by a linear activation layer. These modified U-NETs are called mU-NETs. Several structures have been tested for the prediction of J_0^* and R_s^* . The ones that yielded the best results were empirically found to be one with the same backbone as the original U-NET for J_0^* and a modified version for R_s^* presented in Figure 3c.

It must be emphasized that in our case, the input is 3D and the output is 2D. We however use 2D convolutional layers (2D convolutional networks) because 3D convolutional networks require large memory and computation resources, present higher time costs than 2D CNNs, and are prone to overfitting [48–51].

5.3.2.2 | Generation of the Synthetic Training Datasets. mU-NET takes a data cube as input and predicts either a R_s^* or a J_0^* map.

To create the training and test datasets, we use the results of the NLLS fits on the same experimental samples as in Section 5.3.1.2. The parameter maps are modified before creating the resulting synthetic ELV data cubes.

The results of NLLS fits on the busbar areas are aberrant, and in the synthetic dataset, we put the matching R_s^* and J_0^* to very low values. Likewise, the values of the very small R_s^* and J_0^* outliers are increased because they are likely due to an erroneous fit

on a noisy signal. A rotation between -15° and $+15^\circ$ is applied on the parameter maps, both to increase the dataset size and to make the ML models robust to orientation changes. Finally, to increase the diversity of images originating from the same map, random modifications of R_s^* and J_0^* are applied by multiplying each value by a factor $f \in [0.99, 1.01]$ randomly generated using a uniform distribution.

The dataset consists of 105 data cubes, each sized at $492 \times 495 \times 28$ voxels, along with the parameter maps. The training dataset comprises 82 data cubes, the validation dataset comprises 21 data cubes and the test dataset comprises 2 data cubes. Because each data cube corresponds to an entire cell, a wide variety of patterns are present within a single data cube. Thus, using only two data cubes for the test dataset allows for the estimation of the models' prediction performance across a sufficiently broad range of R_s^* and J_0^* values.

5.3.3 | ML Models Training Time

The ML models have been trained on a personal computer with eight cores and a CPU speed of 2.5 GHz. The training time was of the order of 35–40 h for mU-NET and was comprised between 30 (for R_s^*) and 120 h (for J_0^*) for the MLP. The codes were not optimized for reducing training time, and no specific efforts were made to enhance parallelization. The reported training times are provided for indicative purposes only.

Author Contributions

Erell Laot: formal analysis, methodology, software, visualization, writing – original draft, writing – review and editing. **Jean-Baptiste Puel:** methodology, conceptualization, supervision, validation, writing – review and editing. **Jean-François Guillemoles:** methodology, conceptualization, supervision, validation, writing – review and editing. **Daniel Ory:** methodology, conceptualization, supervision, validation, investigation, data curation, software, writing – review and editing.

Conflicts of Interest

The authors declare no conflicts of interest.

Data Availability Statement

The data supporting the findings of this study are available from the corresponding author upon reasonable request.

References

- W. Wang, A. C.-F. Liu, H. S.-H. Chung, R. W.-H. Lau, J. Zhang, and A. W.-L. Lo, "Fault Diagnosis of Photovoltaic Panels Using Dynamic Current-Voltage Characteristics," *IEEE Transactions on Power Electronics* 31, no. 2 (2016): 1588–1599, <http://ieeexplore.ieee.org/document/7088656/>.
- B. Li, C. Delpha, A. Migan-Dubois, and D. Diallo, "Fault Diagnosis of Photovoltaic Panels Using Full I-V Characteristics and Machine Learning Techniques," *Energy Conversion and Management* 248 (2021): 114785, <https://linkinghub.elsevier.com/retrieve/pii/S0196890421009614>.
- Y. Liu, K. Ding, J. Zhang, et al., "Fault Diagnosis Approach for Photovoltaic Array Based on the Stacked Auto-Encoder and Clustering With I-V Curves," *Energy Conversion and Management* 245 (2021): 114603, <https://linkinghub.elsevier.com/retrieve/pii/S0196890421007792>.
- Z. Chen, L. Wu, S. Cheng, P. Lin, Y. Wu, and W. Lin, "Intelligent Fault Diagnosis of Photovoltaic Arrays Based on Optimized Kernel Extreme Learning Machine and I-V Characteristics," *Applied Energy* 204 (2017): 912–931, <https://linkinghub.elsevier.com/retrieve/pii/S0306261917305214>.
- D. Matusz-Kalasz and I. Bodnar, "Monitoring and Diagnostics of Photovoltaic Cells by Electroluminescence," in *2022 23rd International Carpathian Control Conference (ICCC)* (IEEE, 2022), 158–161, <https://ieeexplore.ieee.org/document/9805888/>.
- A. Gastli, L. Ben-Brahim, and M. B. H. Rhouma, "ANN-Based Extraction Approach of PV Cell Equivalent Circuit Parameters," in *2015 17th European Conference on Power Electronics and Applications (EPE'15 ECCE-Europe)* (IEEE, 2015), 1–10, <http://ieeexplore.ieee.org/document/7311777/>.
- X. Meng, F. Gao, and T. Xu, "A Hybrid Model Parameter Extraction Method for Single-Diode Model of PV Module," in *2020 IEEE Energy Conversion Congress and Exposition (ECCE)* (IEEE, 2020), 3649–3653 en, <https://ieeexplore.ieee.org/document/9235841>.
- X. Hao, P. Liu, Y. Deng, and X. Meng, "A MIC-LSTM Based Parameter Extraction Method for Single-Diode PV Model," *Frontiers in Energy Research* 11 (2024): 1349887, <https://www.frontiersin.org/articles/10.3389/fenrg.2023.1349887/full>.
- J. K. Katahara and H. W. Hillhouse, "Quasi-Fermi Level Splitting and Sub-Bandgap Absorptivity From Semiconductor Photoluminescence," *Journal of Applied Physics* 116, no. 17 (2014): 173504, <https://pubs.aip.org/jap/article/116/17/173504/281390/Quasi-Fermi-level-splitting-and-sub-bandgap>.
- Y. Buratti, Q. T. Le Gia, J. Dick, Y. Zhu, and Z. Hameiri, "Extracting Bulk Defect Parameters in Silicon Wafers Using Machine Learning Models," *npj Computational Materials* 6, no. 1 (2020): 142, <https://www.nature.com/articles/s41524-020-00410-7>.
- M. W. Akram, G. Li, Y. Jin, et al., "CNN Based Automatic Detection of Photovoltaic Cell Defects in Electroluminescence Images," *Energy* 189 (2019): 116319, <https://linkinghub.elsevier.com/retrieve/pii/S0360544219320146>.
- J. Zhang, X. Chen, H. Wei, and K. Zhang, "A Lightweight Network for Photovoltaic Cell Defect Detection in Electroluminescence Images Based on Neural Architecture Search and Knowledge Distillation," *Applied Energy* 355 (2024): 122184.
- L. Lüer, K. Forberich, J. Hepp, et al., "PV Module Power Prediction by Deep Learning on Electroluminescence Images—Assessing the Physics Learned by a Convolutional Neural Network," *Solar Energy Materials and Solar Cells* 264 (2024): 112621, <https://linkinghub.elsevier.com/retrieve/pii/S0927024823004427>.
- O. Breitenstein, A. Khanna, Y. Augarten, J. Bauer, J. M. Wagner, and K. Iwig, "Quantitative Evaluation of Electroluminescence Images of Solar Cells," *Physica Status Solidi (RRL)—Rapid Research Letters* 4, no. 1–2 (2010): 7–9.
- M. Glatthaar, J. Haunschmid, M. Kasemann, J. Giesecke, W. Warta, and S. Rein, "Spatially Resolved Determination of Dark Saturation Current and Series Resistance of Silicon Solar Cells," *Physica Status Solidi (RRL)—Rapid Research Letters* 4, no. 1–2 (2010): 13–15.
- G. Dost, H. Höffler, and J. M. Greulich, "Advanced Series Resistance Imaging for Silicon Solar Cells via Electroluminescence," *Physica Status Solidi (A)* 218, no. 6 (2021): 2000546, <https://onlinelibrary.wiley.com/doi/10.1002/pssa.202000546>.
- Z. Huang, J. W. Ho, K. B. Choi, A. Danner, and K. S. Chan, "Predicting Loss Analysis From Luminescence Images in Si Solar Cells With Convolutional Neural Networks," *Solar RRL* 7, no. 23 (2023): 2300396, <https://onlinelibrary.wiley.com/doi/10.1002/solr.202300396>.
- J. W. Ho, J. Wong, P. T. Christopher Subhodayam, et al., "Device Parameter Extraction for Loss Analysis of Silicon Solar Cells Based on

- Intelligent Model Fitting," *Energy Procedia* 150 (2018): 21–27, <https://linkinghub.elsevier.com/retrieve/pii/S1876610218305526>.
19. B. Chen, J. Peng, H. Shen, et al., "Imaging Spatial Variations of Optical Bandgaps in Perovskite Solar Cells," *Advanced Energy Materials* 9, no. 7 (2019): 1802790, <https://onlinelibrary.wiley.com/doi/10.1002/aenm.201802790>.
 20. A. Delamarre, L. Lombez, and J.-F. Guillemoles, "Contactless Mapping of Saturation Currents of Solar Cells by Photoluminescence," *Applied Physics Letters* 100, no. 13 (2012), <https://pubs.aip.org/apl/article/100/13/131108/23989>Contactless-mapping-of-saturation-currents-of>.
 21. M. P. Peloso, J. Sern Lew, T. Trupke, M. Peters, R. Utama, and A. G. Aberle, "Evaluating the Electrical Properties of Silicon Wafer Solar Cells Using Hyperspectral Imaging of Luminescence," *Applied Physics Letters* 99, no. 22 (2011): 221915, <https://pubs.aip.org/apl/article/99/22/221915/123408/Evaluating-the-electrical-properties-of-silicon>.
 22. D. Ory, N. Paul, and L. Lombez, "Extended Quantitative Characterization of Solar Cell From Calibrated Voltage-Dependent Electroluminescence Imaging," *Journal of Applied Physics* 129, no. 4 (2021): 43106, <https://pubs.aip.org/jap/article/129/4/043106/1078980/Extended-quantitative-characterization-of-solar>.
 23. A. Sharma, A. Sharma, M. Averbukh, et al., "Performance Investigation of State-of-the-Art Metaheuristic Techniques for Parameter Extraction of Solar Cells/Module," *Scientific Reports* 13, no. 1 (2023): 11134, <https://www.nature.com/articles/s41598-023-37824-4>.
 24. V. M. Le Corre, T. S. Sherkar, M. Koopmans, and L. J. A. Koster, "Identification of the Dominant Recombination Process for Perovskite Solar Cells Based on Machine Learning," *Cell Reports Physical Science* 2, no. 2 (2021): 100346, <https://linkinghub.elsevier.com/retrieve/pii/S266638642100031X>.
 25. W. L. Lo, H. S. H. Chung, R. T. C. Hsung, H. Fu, and T. W. Shen, "PV Panel Model Parameter Estimation by Using Neural Network," *Sensors* 23, no. 7 (2023): 3657, <https://www.mdpi.com/1424-8220/23/7/3657>.
 26. O. Ronneberger, P. Fischer, and T. Brox, "U-Net: Convolutional Networks for Biomedical Image Segmentation," (2015), arXiv:1505.04597 [cs].
 27. G. Urbanos, A. Martín, G. Vázquez, et al., "Supervised Machine Learning Methods and Hyperspectral Imaging Techniques Jointly Applied for Brain Cancer Classification," *Sensors* 21, no. 11 (2021): 3827, <https://www.mdpi.com/1424-8220/21/11/3827>.
 28. Z. Zhong, J. Li, Z. Luo, and M. Chapman, "Spectral-Spatial Residual Network for Hyperspectral Image Classification: A 3-D Deep Learning Framework," *IEEE Transactions on Geoscience and Remote Sensing* 56, no. 2 (2018): 847–858, <http://ieeexplore.ieee.org/document/8061020/>.
 29. I. Demir, K. Koperski, D. Lindenbaum, et al., "DeepGlobe 2018: A Challenge to Parse the Earth Through Satellite Images," in *2018 IEEE/CVF Conference on Computer Vision and Pattern Recognition Workshops (CVPRW)* (IEEE, 2018), 172–17209, <https://ieeexplore.ieee.org/document/8575485/>.
 30. H. Ning, Z. Li, C. Wang, and L. Yang, "Choosing an Appropriate Training Set Size When Using Existing Data to Train Neural Networks for Land Cover Segmentation," *Annals of GIS* 26, no. 4 (2020): 329–342, <https://www.tandfonline.com/doi/full/10.1080/19475683.2020.1803402>.
 31. Z. Su, E. Decencière, T.-T. Nguyen, et al., "Artificial Neural Network Approach for Multiphase Segmentation of Battery Electrode Nano-CT Images," *npj Computational Materials* 8, no. 1 (2022): 30, <https://www.nature.com/articles/s41524-022-00709-7>.
 32. A. S. Kovvali, M. Demant, and S. Rein, "Spatially Resolved Material Quality Prediction Via Constrained Deep Learning," in *2019 IEEE 46th Photovoltaic Specialists Conference (PVSC)* (IEEE, 2019), 3059–3062, <https://ieeexplore.ieee.org/document/8980743>.
 33. M. Battaglia, E. Comi, T. Stadelmann, R. Hiestand, B. Ruhstaller, and E. Knapp, "Deep Ensemble Inverse Model for Image-Based Estimation of Solar Cell Parameters," *APL Machine Learning* 1, no. 3 (2023): 36108, <https://pubs.aip.org/aml/article/1/3/036108/2904738/Deep-ensemble-inverse-model-for-image-based>.
 34. P. Kunze, J. Greulich, S. Rein, et al., "Efficient Deployment of Deep Neural Networks for Quality Inspection of Solar Cells Using Smart Labeling," in *37th European PV Solar Energy Conference and Exhibition* (2020), 11.
 35. H.-M. Huang, "An Unsupervised Convolutional Neural Network Method for Estimation of Intravoxel Incoherent Motion Parameters," *Physics in Medicine And Biology* 67, no. 21 (2022): 215018, doi:[10.1088/1361-6560/ac9a1f](https://doi.org/10.1088/1361-6560/ac9a1f).
 36. A. Klepaczko, M. Strzelecki, M. Kociolek, E. Eikefjord, and A. Lundervold, "A Multi-Layer Perceptron Network for Perfusion Parameter Estimation in DCE-MRI Studies of the Healthy Kidney," *Applied Sciences* 10, no. 16 (2020): 5525, <https://www.mdpi.com/2076-3417/10/16/5525>.
 37. B. Hanin, "Universal Function Approximation by Deep Neural Nets With Bounded Width and ReLU Activations," *Mathematics* 7, no. 10 (2019): 992, <https://www.mdpi.com/2227-7390/7/10/992>.
 38. K. Hornik, "Approximation Capabilities of Multilayer Feedforward Networks," *Neural Networks* 4, no. 2 (1991): 251–257.
 39. Z. Lu, H. Pu, F. Wang, Z. Hu, and L. Wang, "The Expressive Power of Neural Networks: A View From the Width," (2017), arXiv:1709.02540 [cs].
 40. Z. Wang, A. C. Bovik, H. R. Sheikh, and E. P. Simoncelli, "Image Quality Assessment: From Error Visibility to Structural Similarity," *IEEE Transactions on Image Processing* 13, no. 4 (2004): 600–612, <http://ieeexplore.ieee.org/document/1284395/>.
 41. J. Wong and M. A. Green, "From Junction to Terminal: Extended Reciprocity Relations in Solar Cell Operation," *Physical Review B* 85, no. 23 (2012): 235205, <https://link.aps.org/doi/10.1103/PhysRevB.85.235205>.
 42. D. Hinken, K. Ramspeck, K. Bothe, B. Fischer, and R. Brendel, "Series Resistance Imaging of Solar Cells by Voltage Dependent Electroluminescence," *Applied Physics Letters* 91, no. 18 (2007): 182104, <https://pubs.aip.org/apl/article/91/18/182104/119496/Series-resistance-imaging-of-solar-cells-by>.
 43. C. J. Shallue, J. Lee, J. Antognini, J. Sohl-Dickstein, R. Frostig, and G. E. Dahl, "Measuring the Effects of Data Parallelism on Neural Network Training," (2019), arXiv:1811.03600v3 [cs.LG].
 44. P. Virtanen, R. Gommers, T. E. Oliphant, et al., "SciPy 1.0: Fundamental Algorithms for Scientific Computing in Python," *Nature Methods* 17 (2020): 261–272.
 45. "scipy.optimize.least_squares—scipy v1.13.0 Manual," accessed April 10, 2024, https://docs.scipy.org/doc/scipy/reference/generated/scipy.optimize.least_squares.html.
 46. S. Yang, W. Hui, L. Chao, et al., "Toward a Diagnostic Method for Efficient Perovskite Solar Cells Based on Equivalent Circuit Parameters," *Journal of Physical Chemistry C* 127, no. 12 (2023): 5663–5675, <https://pubs.acs.org/doi/10.1021/acs.jpcc.2c08601>.
 47. E. Velilla, J. B. Cano, K. Jimenez, J. Valencia, D. Ramirez, and F. Jaramillo, "Numerical Analysis to Determine Reliable One-Diode Model Parameters for Perovskite Solar Cells," *Energies* 11, no. 8 (2018): 1963, <https://www.mdpi.com/1996-1073/11/8/1963>.
 48. S. Mittal, "A Survey of Accelerator Architectures for 3D Convolution Neural Networks," *Journal of Systems Architecture* 115 (2021): 102041.
 49. C. Yu, R. Han, M. Song, C. Liu, and C.-I. Chang, "A Simplified 2D-3D CNN Architecture for Hyperspectral Image Classification Based on Spatial-Spectral Fusion," *IEEE Journal of Selected Topics in Applied Earth Observations and Remote Sensing* 13 (2020): 2485–2501.

50. S. Xie, C. Sun, J. Huang, Z. Tu, and K. Murphy, "Rethinking Spatio-temporal Feature Learning: Speed-Accuracy Trade-Offs in Video Classification," (2018), arXiv:1712.04851 [cs].

51. S. Ghaderizadeh, D. Abbasi-Moghadam, A. Sharifi, N. Zhao, and A. Tariq, "Hyperspectral Image Classification Using a Hybrid 3D-2D Convolutional Neural Networks," *IEEE Journal of Selected Topics in Applied Earth Observations and Remote Sensing* 14 (2021): 7570–7588.

Supporting Information

Additional supporting information can be found online in the Supporting Information section.